Improved visualization of X-ray phase contrast volumetric data through artifact-free integrated differential images

Lorenzo Massimi

Department of Medical Physics and Biomedical Engineering, University College London, Gower St, London WC1E 6BT, UK

Savvas Savvidis

Department of Medical Physics and Biomedical Engineering, University College London, Gower St, London WC1E 6BT, UK

Marco Endrizzi

Department of Medical Physics and Biomedical Engineering, University College London, Gower St, London WC1E 6BT, UK

Alessandro Olivo

Department of Medical Physics and Biomedical Engineering, University College London, Gower St, London WC1E 6BT, UK

Abstract

Artefacts arising when differential phase images are integrated is a common problem to several X-ray phase-based experimental techniques. The combination of noise and insufficient sampling of the high-frequency differential phase signal leads to the formation of streak artifacts in the projections, translating into poor image quality in the tomography slices. In this work, we apply a non-iterative integration algorithm proven to reduce streak artifacts in planar (2D) images to a differential phase tomography scan. We report on how the reduction of streak artifacts in the projections improves the quality of the tomography slices, especially in the directions different from the tomography reconstruction plane. Importantly, the method is compatible with large tomography datasets in terms of computation time.

Keywords: X-ray phase contrast tomography, Differential phase integration, Edge illumination

1. Introduction

Significant effort has been dedicated to the development of X-ray phase imaging systems compatible with conventional X-ray sources, to enable the implementation of these techniques outside specialised facilities such as synchrotrons. At present, several approaches have been established, such as gratings-based and edge illumination which are both starting to move towards clinical applications [1, 2, 3, 4]. Both these techniques belong to the family of "differential" phase imaging methods, providing access to signals the intensity of which depends on the first derivative of the phase [1, 3]. An integration step is therefore needed to retrieve an image where the intensity is proportional to the phase; this is a fundamental step for computed tomography (CT) reconstruction as required by the Fourier slice theorem [5]. In addition, since phase sensitivity is usually achieved in one direction, e.g. perpendicular to the direction of apertures in edge illumination, the derivative is unidirectional [6]. The integration of unidirectional differential phase contrast (DPC) images usually leads to images affected by streak artifacts, resulting from noise and non perfect phase sampling. This is a common problem affecting all DPC with unidirectional sensitivity. Several approaches have been proposed to solve this problem, mainly based on iterative regularized integration [7, 8, 9]. In these methods, the integrated image is obtained as the image the first derivative of which minimizes the difference with the experimental differential phase profile. While they provide good image quality, they also require long computation times that, especially for large images, can be in the order of minutes, preventing their application to CT datasets consist-

ing of thousands of projections. We recently proposed an integration method based on the application of the Wiener filter to unidirectional X-ray DPC images [10], inspired by optical differential interference microscopy [11]. This approach is found to deliver images of quality similar to iterative methods, but in a shorter time, which makes it suitable for application to large CT datasets [10]. It is worth noting that, while both approaches minimize an error function, in Wiener integration the solution is obtained through the application of a filter to the original image which makes this approach non iterative and, therefore, very fast [12].

In this work, we present the application of such a method to the integration of a DPC CT scan of a biological sample obtained through an edge illumination system [2]. We compare the proposed Wiener-based integration approach to an equally fast method based on the Hilbert transform, to demonstrate the advantage in volumetric visualization provided by CT phase contrast datasets obtained from artifact-free integrated DPC projections. The use of Wiener integration reduces the low frequency noise in the CT plane, while proving artefact-free reslices in off-plane orientations that are otherwise affected by severe streak artifacts. We expect this will provide a more reliable estimate of sample density and simplify image segmentation.

2. Methods

2.1. Algorithm

In the following, we briefly introduce the integration algorithm used in the present work. A DPC image features pixel values proportional to the refraction angle $\Delta\theta$ at the pixel location (x,y):

$$\Delta\theta(x, y) \sim \frac{\phi(x + \Delta x, y) - \phi(x, y)}{\Delta x} \qquad (1)$$

where Δx is the image pixel in the horizontal direction and $\phi(x, y) = \int \delta(x, y, z)dz$, where $\delta(x, y, z)$ is the unit decrement of the real part of the complex refractive index, and the integral is taken over the sample thickness. Equation 1 can be written as the convolution of $\phi(x, y)$ with the difference between two Dirac's delta functions shifted by $\Delta x/2$:

$$D(x, y) = \delta(x - \Delta x/2, y) - \delta(x + \Delta x, y) \qquad (2)$$

Therefore, taking the Fourier transform of both sides of eq.2 leads to the equation:

$$\Delta\Theta(u, v) = G(u, v)\Delta\Phi(u, v) \qquad (3)$$

where $\Delta\Theta(u, v)$, $G(u, v)$ and $\Delta\Phi(u, v)$ are the Fourier transforms of the experimental DPC image $\Delta\theta(x, y)$, of

the combination of Dirac's functions $D(x, y)$, and of the phase image $\phi(x, y)$, respectively. $G(u, v)$ can be calculated analytically, yielding $G(u, v) = 2i \sin(2\pi\Delta x\, u)$ (with i the imaginary unit).

A least square estimate solution for $\phi(x, y)$ is given by:

$$\Phi(u, v) = W(u, v)\Delta\Theta(u, v) \qquad (4)$$

where, according to [12], $W(u, v)$ is the Wiener filter, defined as:

$$W(u, v) = \frac{G(u, v)^*}{|G(u, v)|^2 + 1/SNR(u, v)} \qquad (5)$$

where $*$ identifies the complex conjugate and $SNR(u, v)$ is the signal-to-noise ratio as a function of the spatial frequencies, namely the ratio between the modulation transfer function and the noise power spectrum. The use of the Wiener filter prevents the increase of noise and possible discontinuity issues that would be encountered by applying a simple division by $G(u, v)$ to eq.3 to obtain $\Delta\Phi(u, v)$. The Wiener filter requires, by definition, the frequency-dependent signal-to-noise ratio of the estimated image. However, since $SNR(u, v)$ is usually unknown, it is approximated by a function providing a control over the frequency content of the output image $\Phi(u, v)$. The use of a Gaussian is presented in [11], while in this work the Butterworth filter is used due to its better response to high frequencies [7, 13]. The Butterworth filter used in this work was defined as $SNR(u, v) = s/\left(1 + (v/v_0)^{2n}\right)$ where v_0 is the vertical cutoff frequency, n is an integer, s the filter amplitude and v the frequencies in the vertical direction [10].

The integration method discussed above (referred to as Wiener integration hereafter) is compared to an integration approach based on the Hilbert transform, which can be easily implemented during the back projection operation. The Hilbert transform acts in Fourier space by changing the sign of negative frequency components only, thus making image features symmetric and removing the black and white fringes occurring at the edge of features in differential phase images [14].

2.2. Experimental setup and data acquisition

The CT scans of the investigated specimens have been carried out using an edge illumination system based on a Rigaku 007 molybdenum rotating anode source, operated at 40 kVp and 20 mA. A schematic view of the setup is presented in Fig.1(a). The edge illumination system is based on the use of two masks with regular apertures, placed immediately before the sample and in front of the detector. The pre-sample had 78/12
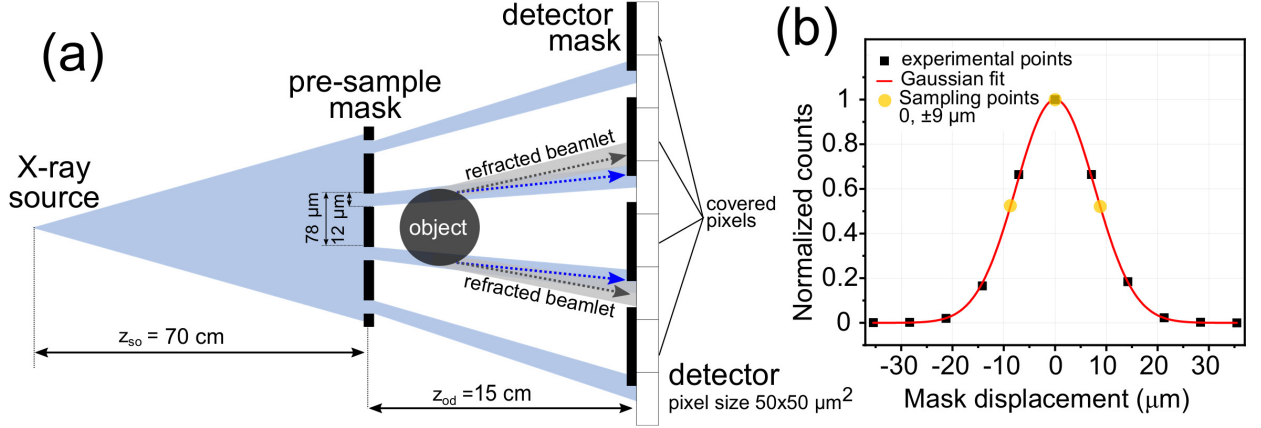
Figure 1: Panels (a) and (b) show a schematic view of the edge illumination system used for acquiring the images and the corresponding sensitivity curve (illumination curve), respectively.

μm pitch/aperture sizes, while the detector mask being a scaled up replica based on a system geometric magnification of 1.2× defined as $(z_{so} + z_{od})/z_{so}$, where z_{so} and z_{od} are the source-to-object and object-to-detector distances, respectively (see Fig.1(a)). In the system used to acquire the presented data $z_{so} = 70$ cm and $z_{od} = 15$ cm. The pre-sample mask shapes the main beam in a series of beamlets while the latter creates unsensitive regions in between the pixels. As each beamlets pass through the sample the change in intensity recorded by each pixel x in the detector column y can be described as:

$$I(x, y) = I_0 T(x, y) IC(x - \Delta x, y) \qquad (6)$$

where I_0 is the beam intensity passing through the pre-sample mask, $T(x, y)$ is the sample transmission function and $IC(x - \Delta x, y)$ is the shifted edge illumination intensity transmission function, which depends on the relative mask displacement. This quantity is usually referred to as illumination curve (IC) and establishes a quantitative relation between a change in the beamlet's position and the measured relative intensity change. The illumination curve obtained with the present system is shown in Fig.1(b). The quantities $T(x, y)$ and Δx are related to the imaginary β and real δ parts of the refractive index, respectively. In particular:

$$T(x, y) = e^{-\int \mu(x,y,z)dz} \qquad (7)$$

where $\mu = (4\pi/\lambda)\beta$ and λ is the wavelength of the incident radiation. Assuming small refraction angles it is possible to write:

$$\Delta x \sim z_{od} \nabla_x \int \delta(x, y, z)dz \qquad (8)$$

where ∇_x is the gradient in the sample mask plane and perpendicular to the direction of the apertures. In both equations the integral is taken across the sample thickness. For simplicity, the effect of scattering is neglected here [15]. Eq.6 represents the basis for the phase retrieval. Assuming a Gaussian approximation for the illumination curve, it can be written for any pixel and for any mask relative position s_i of the masks:

$$I(x, y, s_i)/I_0 = T(x, y) \frac{A_{IC}}{\sqrt{2\pi}\sigma_{IC}} e^{-(s_i - \Delta x)^2/(2\sigma_{IC}^2)} \qquad (9)$$

where A_{IC} and σ_{IC} are the amplitude and width of the IC without the sample. By acquiring at least two images at different positions on illumination curve, i.e. different relative mask displacement, a system of equations is obtained, which can be solved at each pixel location for both $T(x, y)$ and Δx [15].

The detector is a flat panel with pixel size 50×50 μm^2. According to a detector mask period of about 100 μm every other detector column is therefore illuminated by the radiation transmitted through the mask apertures, in what is referred to as the "skipped masks" edge illumination configuration [16]. This configuration has the advantage of reducing the signal diffusion into the scintillator layer, usually referred to as cross-talk, which is typical of indirect conversion detectors. However, in this configuration spatial resolution is limited to the pre-sample mask period, which is $78\mu m$, since nothing in between mask apertures is imaged. In order to address this limitation, additional images are acquired while shifting the sample in sub-period steps in the horizontal direction. The acquisition and digital recombination of multiple dithered images combined with skipped masks leads to a resolution level limited by the size of

3

the apertures in the pre-sample mask [17].

The tomography scan has been performed by acquiring 1000 projections over 360 degrees with an integration time of 1.2 s each. For each angular step, three images at different positions on the illumination curve, ±9 and 0 μm where 0 represents the position at which the apertures in both masks are perfectly aligned, have been acquired and used for the phase retrieval (see Fig.1(b)). In addition, for each projection, 8 additional images were acquired in agreement with dithering oversampled acquisition. The recombination of these images leads to an effective pixel size of 12.5 μm in the CT plane. The combination of multi-points and dithering acquisition results in the 24 images per projection.

The phase retrieval algorithm returns the change in the beamlet position as a consequence of refraction, which is usually referred to as differential phase as described by Eq.8. To recover the integral of phase coefficient across sample thickness integration is needed. Phase integration has been performed with both methods presented in the previous section on each projection before CT reconstruction. Wiener integration has been used with the following parameters for the Butterworth filter: $v_0 = 9 \cdot 10^{-3}\ mm^{-1}$, $n = 1$ and $s = 2 \cdot 10^6$.

2.3. Sample preparation

The samples used in this work are native and decellularized (i.e. cell-free scaffolds) oesophagi obtained from piglets. Animals have been sacrificed in accordance with Schedule One of The Animals (Scientific Procedures) Act 1986 amendment regulations 2012. Native refers to a sample in its natural state as extracted from a piglet, whilst the decellularized is obtained through the decellularization of a native sample in accordance to the established detergent-enzymatic treatment (DET) protocol [18, 19]. Both samples were fixed in 4% paraformaldehyde (PFA) for a 24h period and stored at 4°C. Following PFA fixation the samples were dehydrated in graded ethanol-water cycles up to 100% ethanol and critically point dried using CO_2.

3. Results and discussion

To illustrate the advantages provided by the integration of differential CT projections using the Wiener approach, a comparison with the conventional Hilbert integration is shown on the reconstructions of two piglet oesophagi in Fig.2. Specifically, a native piglet oesophagus (red square) and a cell-free one (red triangle) are shown. A clear difference in density between the two samples is observed, due to the presence of cells in the native one. In the CT reconstruction plane, the difference between the Hilbert integrated slice (panel (a)) and the Wiener integrated one (panel(b)) is barely visible. The streak artifacts originated by Hilbert integration are averaged out during the filtered back projection procedure since they are different for each sinogram line. However, the difference between the two images shown in panel (c), reveals that the streak artifacts introduced a low frequency noise, which is absent in the Wiener integrated slice. This is also confirmed by line profiles taken across the background and the specimen for both integration methods reported in the inset of panel (c) and showing a more uniform background for the Wiener-integrated dataset. Remarkably, despite Wiener integration being based on the suppression of specific high frequencies, no decrease in fine details is observed compared to the Hilbert integration. The advantages of using Wiener integration on slice quality is made evident by extracting a coronal section from the CT volume. The result of such a reslice operation on Hilbert and Wiener integrated data are shown in Fig.2(d) and (e), respectively. The difference between the two coronal slices is also shown in panel (f). A zoom-in of the region indicated by the red rectangles is shown below each image. Streak artifacts are apparent on both samples, and they affect the cell-free one (red triangle) more severely because of its lower density. Also in this case, the difference between the two slices shown (panel (f)) reveals a negligible loss of detail when using Wiener integration. In terms of computational time, the Wiener integration of a single 560×1032 CT projection takes approximately 50 ms while using a Matlab® implementation of the algorithm running on a workstation based on a CPU Intel® Xeon®Gold 6134 3.20GHz. This translates into about 50 seconds to integrate the full CT dataset. In terms of comparison with iterative approaches, it has been already shown that Wiener integration provide similar image quality [10]. However, it is significantly faster. In particular, in comparison to the iterative method proposed in [7], Wiener integration is about three order of magnitude faster to integrate a single projection, which translates into less than a minute to integrate the presented CT dataset, while it would take several days with the iterative approach of reference [7]. For these reasons, a direct comparison on a full CT reconstruction was not attempted here. However, relying on the Fourier transform, artifacts may appear at the edge of the integrated images because of wrapping. This problem can be reduced by zero-padding the image borders before integration. In addition, has been also shown that artifacts occur when the original differential phase signal is poor because of a low SNR or because
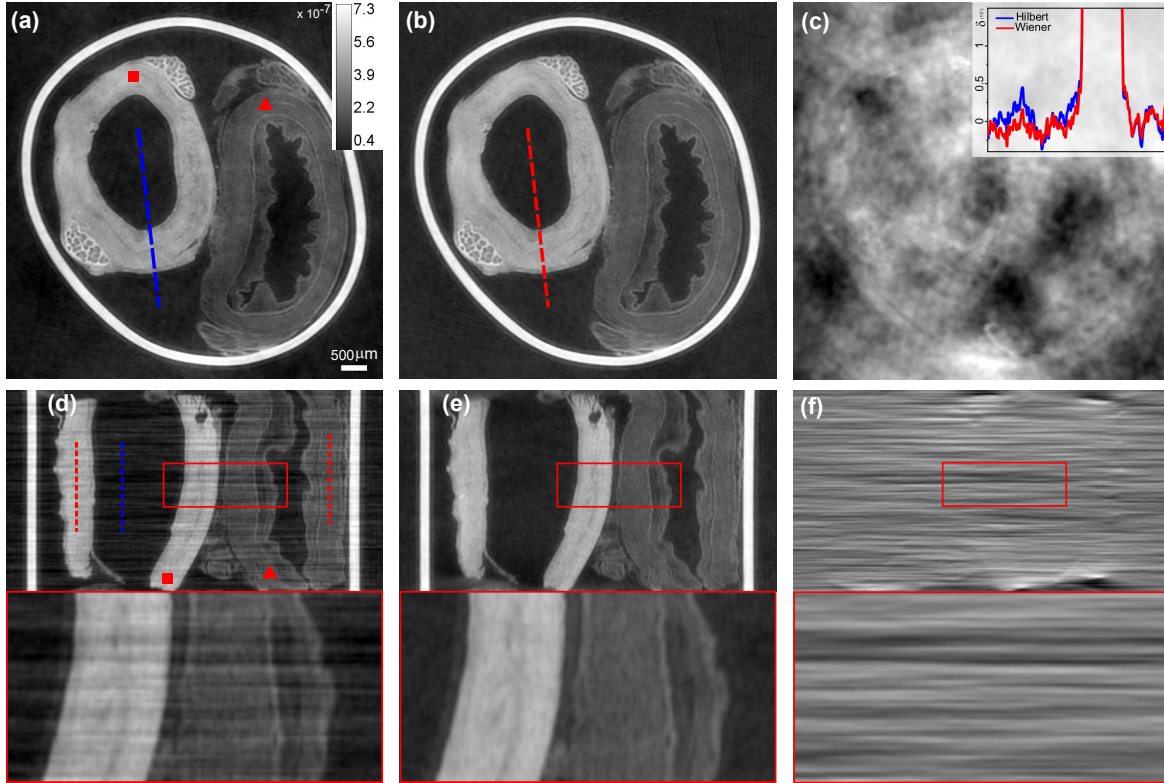
Figure 2: Panels (a) and (b) shows a CT slice obtained from a DPC CT scan integrated using Hilbert and Wiener filters, respectively. Panel (c) shows the difference between them and a line profile across the specimen and the background from both integration methods. The higher intensity part of the profile has been cut to allow appreciating differences in the background region. Panel (d) to (f) shows the same as above but for a coronal reslice of the CT volume. Zoomed-in regions corresponding to red rectangles are reported below each image. In panels (a) and (d) red square and triangle mark a native and a cell-free oesophagus. Dotted lines in panels (d) points at region where lines profiles used in Fig.3 have been extracted. CT images in panels (a),(b),(d) and (e) are shown on the same gray level window.

sample features are almost orthogonal to the direction of the aperture demonstrating that for an accurate quantitative integration a good SNR and a fine sampling step are needed [10, 17].

Density variations across the sample length are a typical metric of interest for tissue engineering specimens, for example to assess the uniformity of the decellularization (and subsequent recellularisation) processes. These can be assessed by extracting line profiles. These are negatively affected by streak artifacts; therefore a more reliable quantification is expected if streak artifacts are effectively suppressed. This point is illustrated by the line profiles shown in Fig.3. A significantly reduced noise is observed when comparing profiles extracted from Wiener-integrated (solid-red lines) to Hilbert-integrated (dashed black lines) coronal slices. This can be quantified by comparing the standard deviation for profiles extracted from both samples (red lines in panel (d)) and the background (blue line in panel (d)). In the first case (native specimen), the stan-

dard deviation is reduced of about a factor 1.5 (from $\sigma_{Hilbert} = 2.9 \cdot 10^{-8}$ to $\sigma_{Wiener} = 1.9 \cdot 10^{-8}$) while in the latter (cell-free specimen), of a factor 2 (from $\sigma_{Hilbert} = 3.2 \cdot 10^{-8}$ to $\sigma_{Wiener} = 1.5 \cdot 10^{-8}$). Finally, a reduction of the background noise, from $\sigma_{Hilbert} = 2.9 \cdot 10^{-8}$ to $\sigma_{Wiener} = 1.1 \cdot 10^{-8}$, is also found (see panel (c)).

4. Conclusions

We have shown how an integration algorithm based on the Wiener filter can be used to integrate thousands of DPC projections obtained from CT scan in an acceptable processing time. The suppression of streak artifacts in the integrated projections translates into a significant improvement of the reconstructed image quality, especially when off-plane slices are considered. We expect the improved image quality provided by Wiener integration to translate into a more reliable estimates of the sample density variations from point to point, which can be used as a non-destructive quality check in tissue
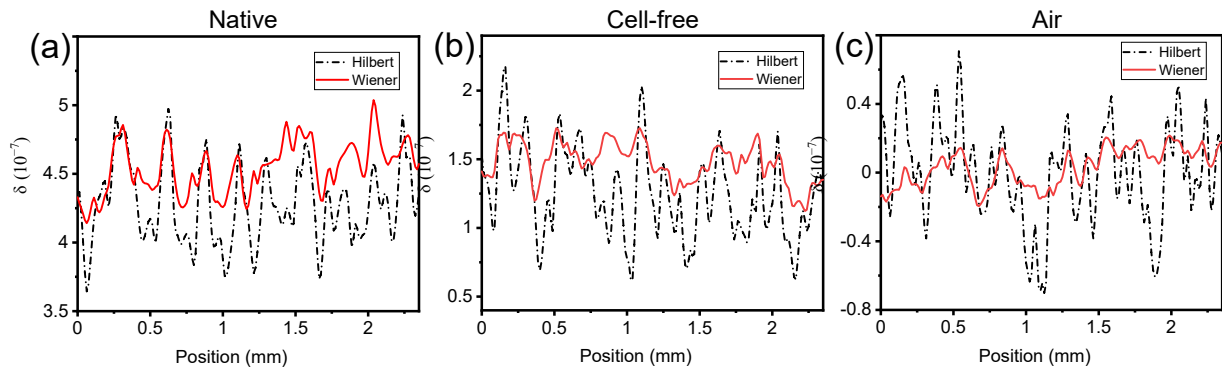
Figure 3: Panels (a) and (b) shows line profiles extracted along the dotted lines reported in coronal view in Fig.2(d) for both the native and cell-free oesophagus. Panel (c) shows line profile extracted from the air region within the specimen (blue dotted line in Fig.2(d)).

engineering. The presented results have been obtained edge illumination, however, Wiener integration can also work with other X-ray phase contrast techniques with unidirectional differential sensitivity, such as gratings or crystal based.

5. Acknowledgments

References

[1] A. Olivo, R. Speller, A coded-aperture technique allowing x-ray phase contrast imaging with conventional sources, Applied Physics Letters 91 (7) (2007) 074106.

[2] L. Massimi, C. K. Hagen, M. Endrizzi, P. R. Munro, G. Havariyoun, P. S. Hawker, B. Smit, A. Astolfo, O. J. Larkin, R. M. Waltham, et al., Laboratory-based x-ray phase contrast ct technology for clinical intra-operative specimen imaging, in: Medical Imaging 2019: Physics of Medical Imaging, Vol. 10948, International Society for Optics and Photonics, 2019, p. 109481R.

[3] F. Pfeiffer, T. Weitkamp, O. Bunk, C. David, Phase retrieval and differential phase-contrast imaging with low-brilliance x-ray sources, Nature physics 2 (4) (2006) 258–261.

[4] F. G. Meinel, F. Schwab, A. Yaroshenko, A. Velroyen, M. Bech, K. Hellbach, J. Fuchs, T. Stiewe, A. Ö. Yildirim, F. Bamberg, et al., Lung tumors on multimodal radiographs derived from grating-based x-ray imaging–a feasibility study, Physica Medica 30 (3) (2014) 352–357.

[5] D. Mihailidis, Computed tomography from photon statistics to modern cone-beam ct, Medical Physics 36 (8) (2009) 3858–3858.

[6] G. K. Kallon, M. Wesolowski, F. A. Vittoria, M. Endrizzi, D. Basta, T. P. Millard, P. C. Diemoz, A. Olivo, A laboratory based edge-illumination x-ray phase-contrast imaging setup with two-directional sensitivity, Applied Physics Letters 107 (20) (2015) 204105.

[7] T. Thüring, P. Modregger, B. R. Pinzer, Z. Wang, M. Stampanoni, Non-linear regularized phase retrieval for unidirectional x-ray differential phase contrast radiography, Optics express 19 (25) (2011) 25545–25558.

[8] J. I. Sperl, D. Bequé, G. P. Kudielka, K. Mahdi, P. M. Edic, C. Cozzini, A fourier-domain algorithm for total-variation regularized phase retrieval in differential x-ray phase contrast imaging, Optics express 22 (1) (2014) 450–462.

[9] M. Nilchian, Z. Wang, T. Thuering, M. Unser, M. Stampanoni, Spline based iterative phase retrieval algorithm for x-ray differential phase contrast radiography, Optics express 23 (8) (2015) 10631–10642.

[10] L. Massimi, I. Buchanan, A. Astolfo, M. Endrizzi, A. Olivo, Fast, non-iterative algorithm for quantitative integration of x-ray differential phase-contrast images, Optics Express 28 (26) (2020) 39677–39687.

[11] E. Van Munster, L. Van Vliet, J. Aten, Reconstruction of optical pathlength distributions from images obtained by a wide-field differential interference contrast microscope, Journal of Microscopy 188 (2) (1997) 149–157.

[12] S. V. Vaseghi, Advanced digital signal processing and noise reduction, John Wiley & Sons, 2008.

[13] C. Raven, Numerical removal of ring artifacts in microtomography, Review of scientific instruments 69 (8) (1998) 2978–2980.

[14] M. Arnison, C. Cogswell, N. Smith, P. Fekete, K. Larkin, Using the hilbert transform for 3d visualization of differential interference contrast microscope images, Journal of microscopy 199 (1) (2000) 79–84.

[15] M. Endrizzi, A. Olivo, Absorption, refraction and scattering retrieval with an edge-illumination-based imaging setup, Journal of Physics D: Applied Physics 47 (50) (2014) 505102.

[16] K. Ignatyev, P. Munro, R. Speller, A. Olivo, Effects of signal diffusion on x-ray phase contrast images, Review of Scientific Instruments 82 (7) (2011) 073702.

[17] P. C. Diemoz, F. A. Vittoria, A. Olivo, Spatial resolution of edge illumination x-ray phase-contrast imaging, Optics express 22 (13) (2014) 15514–15529.

[18] G. Totonelli, P. Maghsoudlou, F. Georgiades, M. Garriboli, K. Koshy, M. Turmaine, M. Ashworth, N. J. Sebire, A. Pierro, S. Eaton, et al., Detergent enzymatic treatment for the development of a natural acellular matrix for oesophageal regeneration, Pediatric surgery international 29 (1) (2013) 87–95.

[19] L. Urbani, C. Camilli, D.-E. Phylactopoulos, C. Crowley, D. Natarajan, F. Scottoni, P. Maghsoudlou, C. J. McCann, A. F. Pellegata, A. Urciuolo, et al., Multi-stage bioengineering of a layered oesophagus with in vitro expanded muscle and epithelial adult progenitors, Nature communications 9 (1) (2018) 1–16.